Available online at www.sciencedirect.com
ScienceDirect
Sensors and Actuators A 136 (2007) 69–79
SENSORS AND ACTUATORS A PHYSICAL
www.elsevier.com/locate/sna

A fast-response microfluidic gas concentrating device for environmental sensing

Sheng Li [a], Jonathan C. Day [b], Jung J. Park [c], Christopher P. Cadou [b], Reza Ghodssi [a,*]

[a] *MEMS Sensors and Actuators Lab, Department of Electrical and Computer Engineering, The Institute for Systems Research, University of Maryland, College Park, MD 20742, USA*
[b] *Department of Aerospace Engineering, University of Maryland, College Park, MD 20742, USA*
[c] *Department of Materials Science and Engineering, University of Maryland, College Park, MD 20742, USA*

Received 12 October 2006; received in revised form 6 November 2006; accepted 19 November 2006
Available online 28 December 2006

Abstract

This paper describes the design, fabrication and characterization of a microfluidic gas centrifuge for separating dilute gas mixtures based on the molecular weights of their constituents. The principal advantage of this approach is its fast response time compared to other methods that are based on permeation or adsorption/desorption. This would allow it to serve as a real-time preconcentrator for improving the sensitivity of miniature chemical sensors. Devices with nozzle throat widths as small as 3.6 μm have been fabricated using photolithography, deep reactive ion etching (DRIE) and silicon-glass anodic bonding. Measurements of the device's performance show that a single stage can achieve a two-fold enrichment of an initially 1% mixture of SF_6 in N_2 in 0.01 ms. These experimental findings are consistent with the results of two-dimensional numerical simulations of the flow through the device. The simulations suggest that the performance of a single stage could be improved significantly by changing the geometry of the entrance flow. Further improvements in performance could be achieved by cascading the devices.
© 2006 Elsevier B.V. All rights reserved.

Keywords: MEMS; Microfluidic device; Gas concentration; Computational fluid dynamics

1. Introduction

On-site quantitative analysis of volatile and semi-volatile chemical vapors is required for environmental monitoring. Normally, detecting chemical vapors relies on labor-intensive and costly sample collection followed by transport to a remote laboratory for analysis. This limits the frequency and overall quality of the measurements [1]. Meanwhile, currently available portable instruments (e.g., miniature mass spectrometers) lack the sensitivity for routine air quality monitoring [2–5]. This deficiency can be rectified by developing miniaturized pre-concentrators that can be used as front-ends for portable instruments.

The temporal response of many commonly used techniques for sensitivity enhancement, like gas chromatography, sorbent beds, and selectively permeable polymer diaphragms [6–11], is limited by the relatively large time constants (∼minutes) associated with adsorption/desorption or permeation of gas molecules. In addition, these techniques require temperature programming and/or consumable materials such as adsorbents that increase the complexity of device fabrication and system integration.

The objective of this work is to demonstrate a fast-response microfluidic gas concentrating device that eliminates the need for embedded electrodes, adsorbents, or membranes. The device can provide simultaneous gas concentration and separation like a centrifuge, but is much easier to be realized at the microscale. While other concentration methods take several to tens of minutes for the absorption/desorption or permeation of the gas molecules being focused, this device exhibits a fast response (<0.01 ms) suitable for use as a real-time preconcentrator in miniaturized chemical sensing systems.

This paper describes the design, fabrication, and characterization of a single-stage gas concentration device. The basic

* Corresponding author.
E-mail address: ghodssi@umd.edu (R. Ghodssi).

0924-4247/$ – see front matter © 2006 Elsevier B.V. All rights reserved.
doi:10.1016/j.sna.2006.11.035

operating principle is described, design considerations are discussed, and the fabrication process is described. Experimental procedures for measuring the device's ability to concentrate heavy gas molecules (like volatile organic vapors) under atmospheric conditions are developed based on mass spectrometry. Measurements of the device's performance are compared to the predictions of a two-dimensional computational fluid dynamics (CFD) simulation. Taken together, these results are used to develop a quantitative understanding of the separation processes occurring in the device and how the performance of the device could be improved by changing its design.

2. Design and fabrication

2.1. Operating principle

The operation of the gas concentrating device is based on the separation nozzle method originally developed for the enrichment of the uranium isotope ^{235}U [12–14] where a gas mixture is divided into fractions of different compositions [14] in a continuous process. Fig. 1a is a 3-D contour image of the single-stage gas separation device. It consists of a curved converging-diverging nozzle, a deflection wall, and a skimmer. A gas mixture (e.g., SF_6 diluted in N_2) is introduced on the left side of the image at the entrance to the curved nozzle. The mixture is accelerated by expansion in the nozzle and then deflected by the curved channel. The centripetal acceleration associated with the turning flow creates a radial pressure gradient that drives differential diffusion of N_2 and SF_6 in directions perpendicular to the streamlines. The heavier SF_6 molecules become concentrated at the periphery of the flow field and a skimmer is used to mechanically separate the stratified gas mixture exiting the curved channel into a 'heavy' fraction that is enriched in SF_6 and a 'light' fraction that is depleted in SF_6 [15].

2.2. Separation factor

The shift in concentrations between the light and the heavy fractions is characterized by the separation factor A which is usually expressed in terms of partial cuts θ_i. The partial cut of a component of the mixture is the percentage of its throughput in the separation element which is withdrawn in the light fraction stream [14]. For a simple binary gas mixture, A is defined as

$$A = \frac{\theta_l(1-\theta_h)}{\theta_h(1-\theta_l)} \quad (1)$$

where θ_l and θ_h are respectively the light component and heavy component partial cuts. The partial cuts can be written in terms of the mass flow rates of the heavy and light species in the heavy and light streams as follows:

$$\theta_l = \frac{\dot{m}_{l,light}}{\dot{m}_{l,light} + \dot{m}_{l,heavy}} \text{ and } \theta_h = \frac{\dot{m}_{h,light}}{\dot{m}_{h,light} + \dot{m}_{h,heavy}} \quad (2)$$

The first subscript l or h, corresponds to the light species or the heavy species while the second subscript, '*light*' or '*heavy*', corresponds to the light or heavy fraction stream where the species is found. Based on these definitions, perfect separation corresponds to $\theta_h = 0$ and $A \to \infty$. Therefore, the success of the design of a separation device is directly related to its ability to maximize the separation factor.

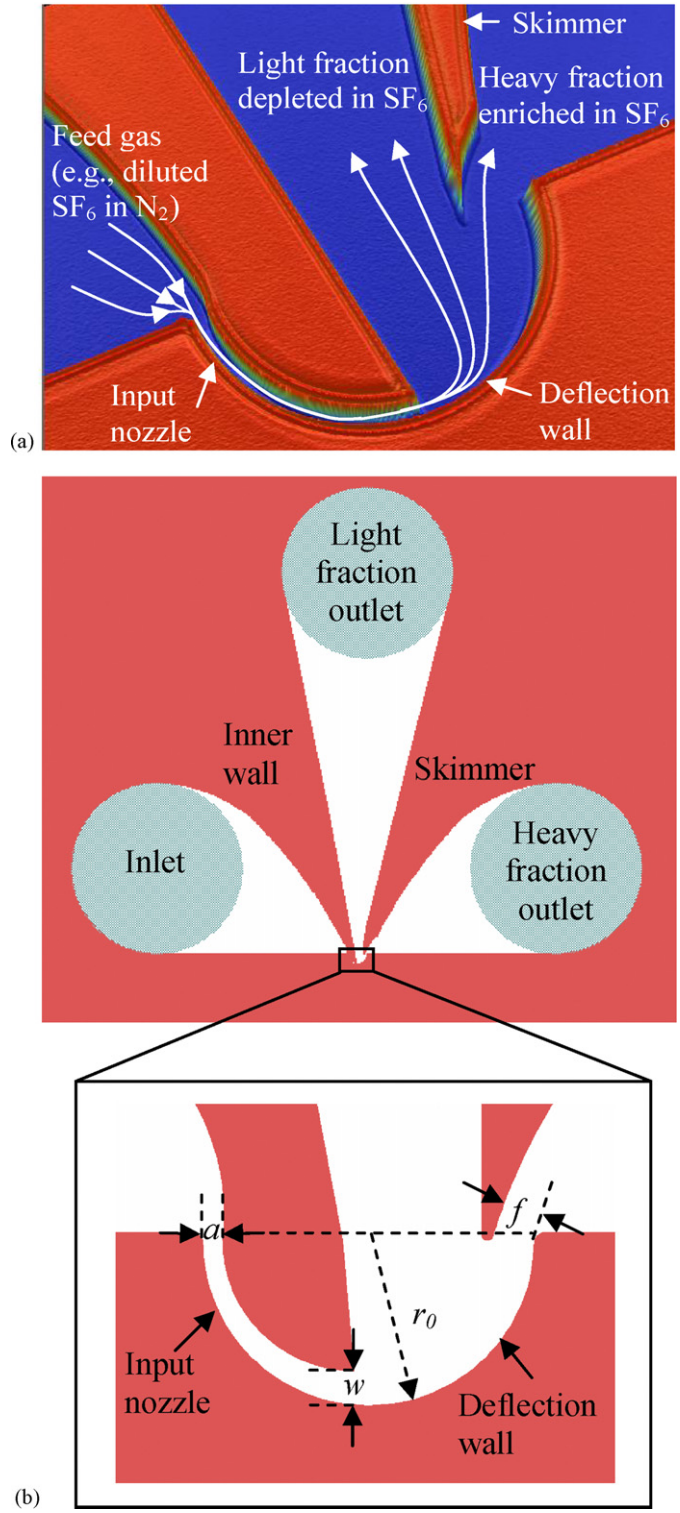

Fig. 1. (a) Three-dimensional optical profilometry surface image of a single-stage gas concentrating element; (b) schematic diagram of a microfabricated single-stage separation device showing the inlet and outlet plenums and a close-up view of the gas concentrating channel identifying the critical design parameters.

2.3. Device design

A schematic diagram of the microfabricated single-stage gas concentrating device is shown in Fig. 1b. The inlet and outlet plenums are 500 μm in diameter and are connected to capillary tubes for gas injection and collection. The close-up view shows the curved converging-diverging nozzle formed by the deflection wall and the inner wall. The critical geometric parameters, like the nozzle throat width a, the nozzle exit width w, the radius of curvature of the deflection wall r_0, and the skimmer distance f (i.e., the width of the channel formed by the skimmer and the deflection wall), are also shown.

Previous studies [12,13] of uranium isotope separation showed that finite values for mixture separation were only obtained when the flow was in the transition regime between continuum and free molecular flow. This regime is identified using the Knudsen number Kn

$$Kn = \frac{\lambda}{d} \tag{3}$$

where λ is the mean free path of gas flow and d is a characteristic dimension of the flow passage. The mean free path, λ, is estimated using the following equation [16]:

$$\lambda = \frac{1.26\mu\sqrt{RT}}{p} \tag{4}$$

where μ is the coefficient of viscosity of the gas mixture, R is the gas constant, p is the pressure, and T is the gas temperature. In this work, p ranges from one to three atmospheres and the nozzle depth d is used as the characteristic dimension of the flow passage. Choosing $d = 5$ μm ensures that $0.005 < Kn < 0.05$ so that the flow remains within the slip regime [17].

One-dimensional isentropic flow relations [16] are used to determine the relationship between the mass flow rate and the nozzle throat

$$a = \frac{\dot{m}}{d\sqrt{\gamma p \rho}}\left(\frac{2}{\gamma+1}\right)^{\frac{\gamma+1}{2(\gamma-1)}} \tag{5}$$

width a assuming that the nozzle throat is choked (i.e. the Mach number at the throat is unity). In this expression, ρ is the gas density and γ is the ratio of specific heats (c_p/c_v) for the gas mixture. For operating pressures of 1 to 3 atmospheres, nozzle widths of 18.0 μm and 3.6 μm are selected to ensure that the mass flow rate is comparable to that of some existing miniaturized mass spectrometers: less than one standard cubic centimeter per second (SCCM). The expansion ratio (i.e., the ratio of exit width w to throat width a) of the nozzle is chosen to be 1.69 which corresponds to a maximum exit Mach number of 2 in the absence of boundary layer growth.

In general, the skimmer should be located as far downstream in the flow path as possible and close to the deflection wall in order to only capture the dense gas molecules concentrated at the periphery of the centrifugal field. In this design, the skimmer distance f is chosen to be 20 μm. The two separation devices that will be evaluated in this study have the same radius of curvature of the deflection wall of 120 μm and the same skimmer distance of 20 μm, but different throat widths of 18.0 μm and 3.6 μm, respectively.

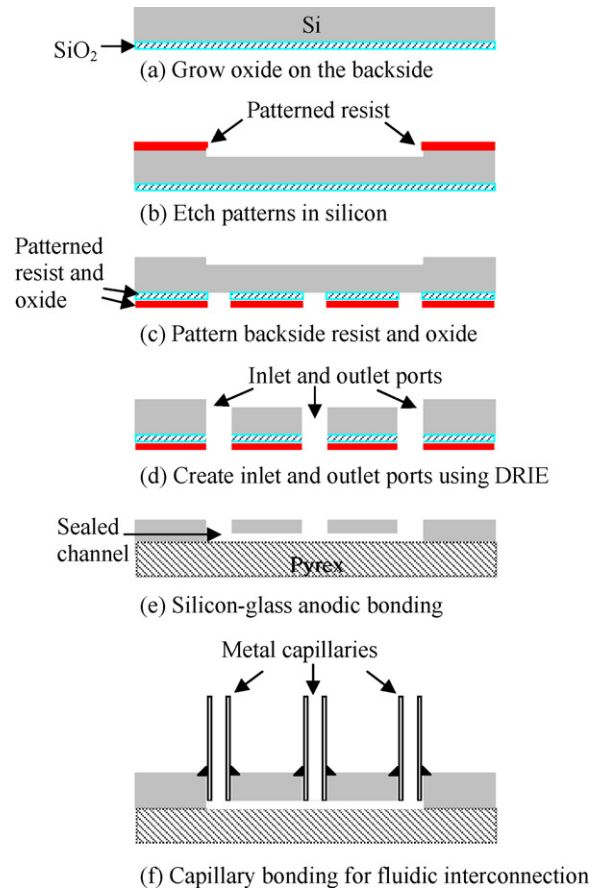

Fig. 2. Device fabrication process including fluidic interconnections.

2.4. Device fabrication

Previously, fabrication of isotope separation devices relied either on stacking of photo-etched metal foils or the LIGA process [12,13,18]. Both processes are tedious and costly. Today, newer microfabrication techniques like deep reactive ion etching (DRIE) and wafer-lever bonding can be used to construct these separation devices much more easily. Fig. 2 shows the process that was developed for fabricating the device pictured in Fig. 1b. The process begins by growing a 2-μm layer of oxide on the backside of a silicon wafer (step a). The next step involves spinning and patterning a 1.5-μm layer of photoresist (S1813, Shipley, Marlborough, MA) on the front side of the wafer, followed by etching 5 μm deep gas concentrating channels in silicon with reactive ion etching (RIE) (step b). A 6-μm masking layer of photoresist (AZ 9245, Clariant, Somerville, NJ) is then spun and patterned to define the inlet and outlet ports, after which the backside oxide is etched with buffered HF (step c). The combination of the patterned photoresist and oxide serves as the etch mask for generating through holes in the silicon substrate with deep reactive ion etching

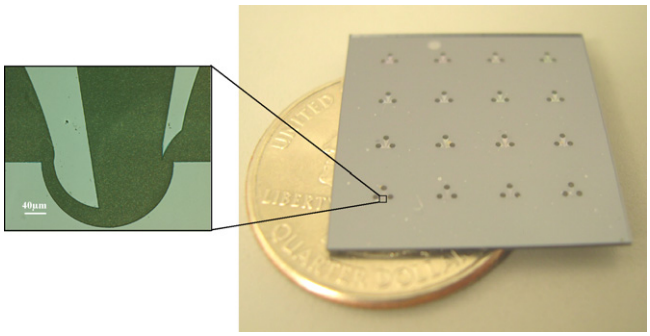

Fig. 3. Optical micrograph of a microfabricated chip after silicon-to-glass anodic bonding with a close-up view of a single-stage separation nozzle.

(DRIE) (step d). Following this step, the resist and oxide are stripped, and the silicon wafer is anodically bonded to a pyrex wafer to seal the microfluidic channels (step e). Finally, metal capillaries are bonded to the inlet/outlet ports in the silicon wafer to realize the microfluidic interfacing (step f). This interconnection process is described in detail elsewhere [19]. Fig. 3 shows a microfabricated chip with a close-up of a gas concentrating device.

3. Gas separation experiments and analysis

Gas separation experiments are conducted to examine the effect of operating conditions and geometric parameters on the performance of the fabricated devices. Two different inert gas mixtures, 1 mol% SF_6/99 mol% N_2 and 1 mol% SF_6/99 mol% Ar, are used in the experiments. The mean molecular weight (MW) of the first mixture is very close to that of air while the MW of SF_6 is close to that of some organic contaminants such as trichloroethylene and naphthalene [1]. This is intended to simulate conditions experienced by a generic miniature chemical sensor. The second mixture is used to study the influence of the molecular weight difference between the heavy component and light components of the mixture on the concentration effect.

Fig. 4 is a schematic diagram of the test apparatus that was used to measure separation performance. Upstream and downstream gas flow rates are controlled and monitored using electronic flow controllers and meters (HFC-302 and HFM-300, Teledyne Hastings Instruments, Hampton, VA). The upstream, light fraction, and heavy fraction pressures are measured using

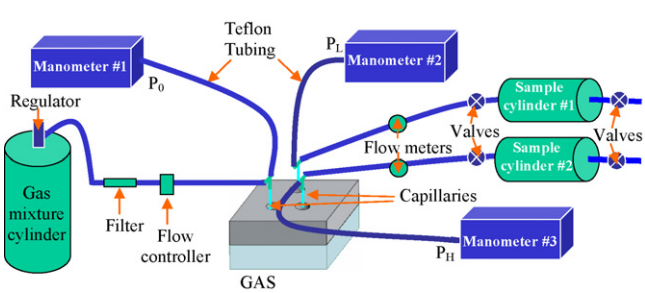

Fig. 4. Schematic of experimental setup for gas separation.

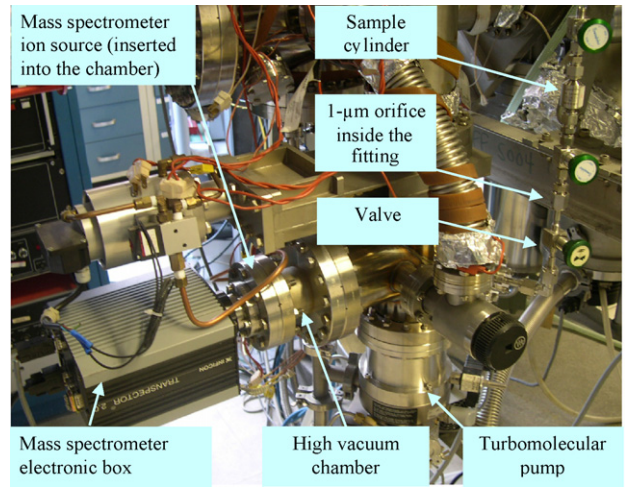

Fig. 5. Photograph of mass spectrometric gas analysis apparatus.

electronic manometers (722A and 622A, MKS Instruments, Andover, MA) connected to the capillary tubes bonded to the device. Two 10-cm^3 sample cylinders (SS-4CD-TW-10, Swagelok, Solon, OH) collect the gas exiting the heavy and light fraction ports. At the conclusion of an experiment, the cylinders are removed and the composition of their contents is determined using mass spectrometry [20].Fig. 5 shows the gas analysis apparatus which consists of a mass spectrometer (Transpector CIS TS200, Inficon, East Syracuse, NY), a vacuum chamber, a turbomolecular pump, and a mechanical pump (not shown in the figure). The sample cylinder is connected to the vacuum chamber through a 1-μm orifice. The orifice limits the gas flow to ensure that adequate vacuum can be maintained for effective electron ionization. The mass spectra of the gas samples are used to determine the concentrations in the samples and the effectiveness of the separation process.

In the mass spectrometric gas analysis, an electron energy of 70 eV was used to ionize gas molecules. At this energy level and at high vacuum, the interaction between electrons and molecules leaves some ions with so much extra energy that they break up to give ions of smaller mass. This fragmentation is characteristic for a given substance [21]. For example, SF_6 molecules are often broken down into 13 different fragment patterns some of which are of negligible intensity compared to the highest fragment peak at mass 127. In our experiments, the six strongest fragments (i.e., masses 127, 89, 108, 129, 51, and 70) are counted to evaluate the concentration of SF_6 in the mixture. Before measuring the separated gas samples, the mass spectrometer was calibrated using pure SF_6 and a known mixture of SF_6/N_2. Uncertainties in the measurements originate from two principal sources: fluctuations in the ion abundances measured by the mass spectrometer and interference from air trapped in the sample cylinder. The former was minimized by taking measurements when the output signal of mass spectrometer was most stabilized. The contribution of N_2 fragmentation patterns from the residual air was inferred by measuring the abundance of O_2 fragments in the separated mixtures, and the ratio of N_2 to O_2, and comparing the results to measurements of air samples.

4. Device modeling

4.1. Governing equations

Convective transport of the bulk fluid is modeled using the 2-D time-invariant, compressible Euler equations [22] plus the equation of state for an ideal gas [23].

$$(\vec{u}\cdot\vec{\nabla})\rho + \rho\vec{\nabla}\cdot\vec{u} = 0 \tag{6}$$

$$(\vec{u}\cdot\vec{\nabla})\vec{u} + \left(\frac{1}{\rho\vec{\nabla}\rho}\right) = 0 \tag{7}$$

$$(\vec{u}\cdot\vec{\nabla})p + \gamma p\vec{\nabla}\cdot\vec{u} = 0 \tag{8}$$

$$p = \rho RT \tag{9}$$

In these expressions, $\vec{u}$ is the velocity vector, γ is the ratio of specific heats (C_p/C_v) for the gas mixture, p is the pressure of the gas mixture, ρ is the density of the gas mixture, T is the temperature, and R is the gas constant. Eq. (6) represents conservation of mass, Eq. (7) represents conservation of momentum, Eq. (8) represents conservation of energy, and Eq. (9) is the equation of state for an ideal gas. These equations remain valid in the slip regime [17].

Fluid flow along the streamlines is driven by the difference in pressure between the inlet and outlet. Centripetal acceleration associated with the deflection of the streamlines through the curved passage re-orients the overall pressure gradient field so that there is a component that is normal to the streamlines. This component is what drives the separation process.

The diffusive transport of individual molecular species is determined by enforcing mass conservation for each component. This takes the following form for non-reacting steady flows [23]:

$$\nabla\cdot(\vec{J}_i + \rho\omega_i\vec{u}) = 0 \tag{10}$$

In this expression, $\vec{J}_i$ is the diffusive flux vector of species i, ρ is the density of the bulk mixture, ω_i is the mass fraction of species i and $\vec{u}$ is the bulk convective velocity. The diffusive flux vector is represented in the numerical simulation using the formulation proposed by Curtiss and Bird [24]

$$\vec{J}_i = -D_i^{\mathrm{T}}\nabla\ln(T) - \rho_i\sum_{j=1}^{N} D_{ij}d_j \tag{11}$$

where D_i^{T} is the thermal diffusion coefficient, T is the thermodynamic temperature, ρ_i is the density of the ith species, and D_{ij} are the symmetric multi-component diffusivities. The diffusion driving force d_j is given by:

$$d_j = \nabla p_j + \omega_j\nabla p - \rho_j g_j + \omega_j\sum_{k=1}^{N}\rho_k g_k \tag{12}$$

where p is the pressure of the mixture, p_j is the partial pressure of the jth species, and g_j and g_k represent any external body forces per unit mass acting on the jth and kth species. Since the gas molecules are not charged, g is the same for all molecules (equal to 9.8 m/s^2) and the last two terms in Eq. (12) sum to zero. Therefore, these two terms do not contribute to the separation process.

It is easier to understand the physics of the separation processes by re-writing Eq. (10) in terms of a 'Fickian' diffusion coefficient D'_{im} for transport of a single species into the gas mixture (denoted by the subscript 'm')

$$\vec{J}_i = -D_i^{\mathrm{T}}\nabla\ln(T) - \rho_i D'_{\mathrm{im}}d_i \tag{13}$$

The relationship between this 'Fickian' diffusion coefficient and the symmetric diffusion coefficient of Eq. (11) is given by [25]:

$$D'_{\mathrm{im}}d_i = -\frac{1}{\bar{W}}\sum_{j\neq i}^{N} W_j D_{ij} d_j \tag{14}$$

In this expression, N is the total number of species in the mixture and $\bar{W}$ is the average molecular weight of the mixture. Inserting Eq. (13) into (14) (and assuming the species are not electrically charged) gives the following expression for the diffusive flux which illustrates the basic physics of the separation process more clearly than Eqs. (11) and (12):

$$\vec{J}_i = -D_i^T\frac{\nabla T}{T} - \rho\omega_i D'_{\mathrm{im}}\left[\nabla x_i + (x_i - \omega_i)\frac{\nabla p}{p}\right] \tag{15}$$

Eq. (15) shows that SF_6 is driven radially outward in the direction of the pressure gradient because $x_{SF_6} - \omega_{SF_6} < 0$. Conversely, N_2 is driven in the opposite direction toward the inner wall of the flow passage because $x_{N_2} - \omega_{N_2} > 0$. The net performance of the device is set by a competition between the pressure gradient force (the second term in the square brackets) which seeks to separate the constituents and the concentration gradient force (the first term in the square brackets) which seeks to bring the constituents back together.

4.2. Boundary conditions

Fig. 6a shows the computational domain over which Eqs. (6)–(12) are solved. At the inlet, the SF_6 and N_2 mass fractions are fixed at 0.05 and 0.95, respectively (corresponding to 1 mol% SF_6 and 99 mol% N_2). The non-dimensional fluid density is 1 and the non-dimensional inlet pressure varies from 1 to 3 atm. The non-dimensional pressure is set to 1 atm at both outlets and the convective flux is required to be normal to the exit areas. No material flux is permitted across any other bounding surface and perfect slip (i.e. no shear stresses) is assumed along all walls.

4.3. Solution method

The governing equations are solved subject to the boundary conditions using a commercially available software package called FEMLAB that implements a finite element method [26]. Fig. 6b is an example of 'typical' finite element mesh consisting of an unstructured grid of triagonal elements. Since FEMLAB uses adaptive gridding, the meshes for each set of flow conditions are different. The software package provides a variety of solvers.

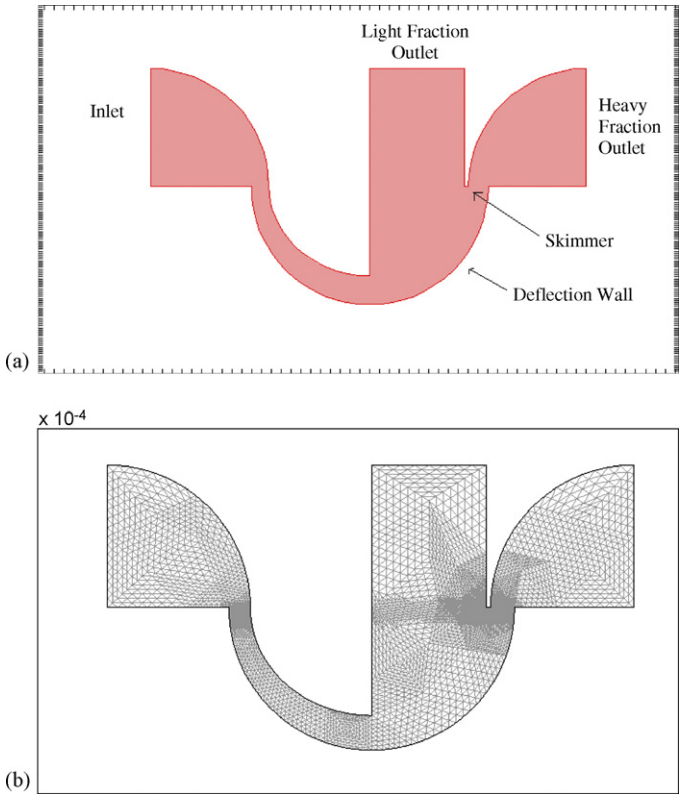

Fig. 6. (a) Computational domain used by the numerical model; (b) a typical finite element mesh for the model geometry with 1/4 of the mesh points displayed.

We use the interative, steady-state non-linear solver because the problem is steady-state and highly non-linear. The solver uses an affine invariant form of the damped Newton method [26] to solve a linearized form of the governing equations [27]. Artificial diffusion is used to help maintain a stable solution throughout the iterative process by damping instabilities. One convenient aspect of FEMLAB is that different types of artificial diffusion can be applied to different governing equations. Isotropic and streamline diffusion are used in the solution of the Euler equations. No artificial diffusion utilized for the solution of the diffusion equation. Isotropic diffusion adds a coefficient of artificial diffusion to the diffusion already in the problem at the location of high gradients. The key advantage of isotropic diffusion is that it is most successful at limiting the impact and magnitude of local instabilities. However, its use also reduces the order of accuracy of the solution from second order to first order in the regions where it is used. Streamline diffusion is added using the upwind Petrov-Galerkin (SUPG) method [26]. The key advantage of this method is that it does not perturb the initial equations so it does not reduce the order of accuracy of the solution.

FEMLAB provides three methods for specifying partial differential equations (PDEs) [26]. These methods are the coefficient, general, and weak forms. The coefficient form is unable to handle highly non-linear functions and therefore will not be discussed as the problem under consideration here is highly non-linear.

4.3.1. General form

The general form is given by writing the PDEs in the following form:

$$\begin{cases} \nabla \cdot \Gamma = \vec{F} & \text{in} \quad \Omega \\ -\vec{n} \cdot \Gamma = \vec{G} + \left(\dfrac{\partial \vec{R}}{\partial u}\right)^T \mu & \text{in} \quad \partial\Omega \\ 0 = \vec{R} & \text{in} \quad \partial\Omega \end{cases} \tag{16}$$

The first equation is the PDE, the second equation is the Neumann boundary condition, and the third equation is the Dirichlet boundary condition. The terms Γ, F, G, and R are coefficients that can be functions of the spatial coordinates, the solution $\vec{u}$, or spatial derivatives of the solution $\vec{u}$. The coefficients F, G, and R are scalar functions, Γ is the flux vector, and μ is the Lagrange multiplier.

4.3.2. Weak form

The weak form begins with the general form, multiplies each term by an arbitrary test function, v, applies Green's formula to complete an integration by parts, and finally substitutes the Neumann boundary equation into the PDE. The resulting equations are:

$$\begin{aligned} 0 &= \int_{\Omega} (\nabla v \cdot \Gamma - vF) dA + \int_{\partial\Omega} v \left(G + \frac{\partial R}{\partial u} \mu \right) ds \\ 0 &= R \quad on \quad \partial\Omega \end{aligned} \tag{17}$$

There are two key advantages to using the weak formulation. The first is the ability of the weak form to handle discontinuities. Since the test function, v, can be any function, it can be used to facilitate finding a solution in the presence of discontinuities. The second advantage is that the weak form guarantees that the solver will use the exact Jacobian. This is possible because the weak form utilizes all of the terms in Eq. (16) when solving for the Jacobian while the general solution only uses the coefficient terms when finding the Jacobian. Further explanations of the general and weak forms along with the respective solution methods may be found elsewhere [28].

5. Results and discussion

5.1. Flow modes

The choice of problem formulation appears to influence the solution to Eqs. (6)–(12) that is found: For identical boundary conditions, the weak formulation leads to a different solution (solution 1) than the general formulation (solution 2). Both solutions satisfy conservation of mass, momentum, and energy and do not violate the second law of thermodynamics. Furthermore, when solution 1 is used as the initial condition for a calculation based on the general formulation, a converged solution identical to solution 1 is returned. Similarly, when solution 2 is used as the initial condition for a calculation based on the weak formulation, a converged solution identical to solution 2 is returned. Therefore, both solutions appear to be physical indiciating that

the flow field must have multiple modes. Additional explanation and verification is presented elsewhere [29].

5.2. Flow structure

Fig. 7a and b show the Mach number distributions and streamlines associated with modes 1 and 2, respectively when the pressure ratio across the device is 1.75. In both modes, large recirculation regions form in the inlet section in order to accommodate the 90° downward turn required to enter the curved nozzle. The resulting flow obstruction causes the flow to begin accelerating while still inside the inlet plenum. The flow continues to accelerate in the nozzle reaching supersonic speeds within the first 1/3 of its length and then decelerating through the remainder of the curved section of the flow path. The average Mach number through most of the curved passage is approximately 0.5. The pressure gradients associated with the acceleration, deceleration, and flow turning can be seen more clearly in Fig. 7c which shows contours of static pressure for mode 1 when the pressure ratio across the device is 1.75.

5.3. Diffusive transport

Fig. 7d shows that SF_6 is driven radially outward through most of the curved flow passage. However, there is a relatively small region near the nozzle entrance where SF_6 is actually driven radially inward. This is because the 90° downward turn of the flow as it enters the nozzle causes the pressure gradient to point radially inward in this region. The pressure gradient reverses direction in the curved section of the nozzle as the flow is turned 180° in the opposite direction (counter-clockwise) and this drives diffusive transport in the proper direction (radially outward) in the device. The simulations show that the region of greatest SF_6 diffusive flux occurs approximately 1/3 of the way through the nozzle where the radial pressure gradient is strongest.

5.4. Separation

Eqs. (1) and (2) are used to compute the separation factor. In the experiments, the partial cut of SF_6 or N_2 is evaluated using the ion abundances of SF_6 and N_2 in the heavy and light fraction streams. In the simulations, the partial cuts are computed using the total mass fluxes of SF_6 and N_2 in the heavy and light streams. These are computed by integrating the respective mass flux distributions along the planes illustrated in Fig. 7d.

Fig. 8 compares mass spectra measured in the heavy and light fraction streams and shows that the separation predicted in the numerical simulations is consistent with experimental measurements. The increase in the total abundance of main SF_6 fragments in the heavy fraction stream (while the total abundance of main N_2 fragments in the heavy fraction is slightly less than light fraction) clearly indicates that enrichment of the heavy fraction stream is occurring.

Fig. 9 shows that the predictions of the numerical simulations are qualitatively consistent with the experimental measurements for device 1 with the nozzle throat width of 18.0 μm: Both show

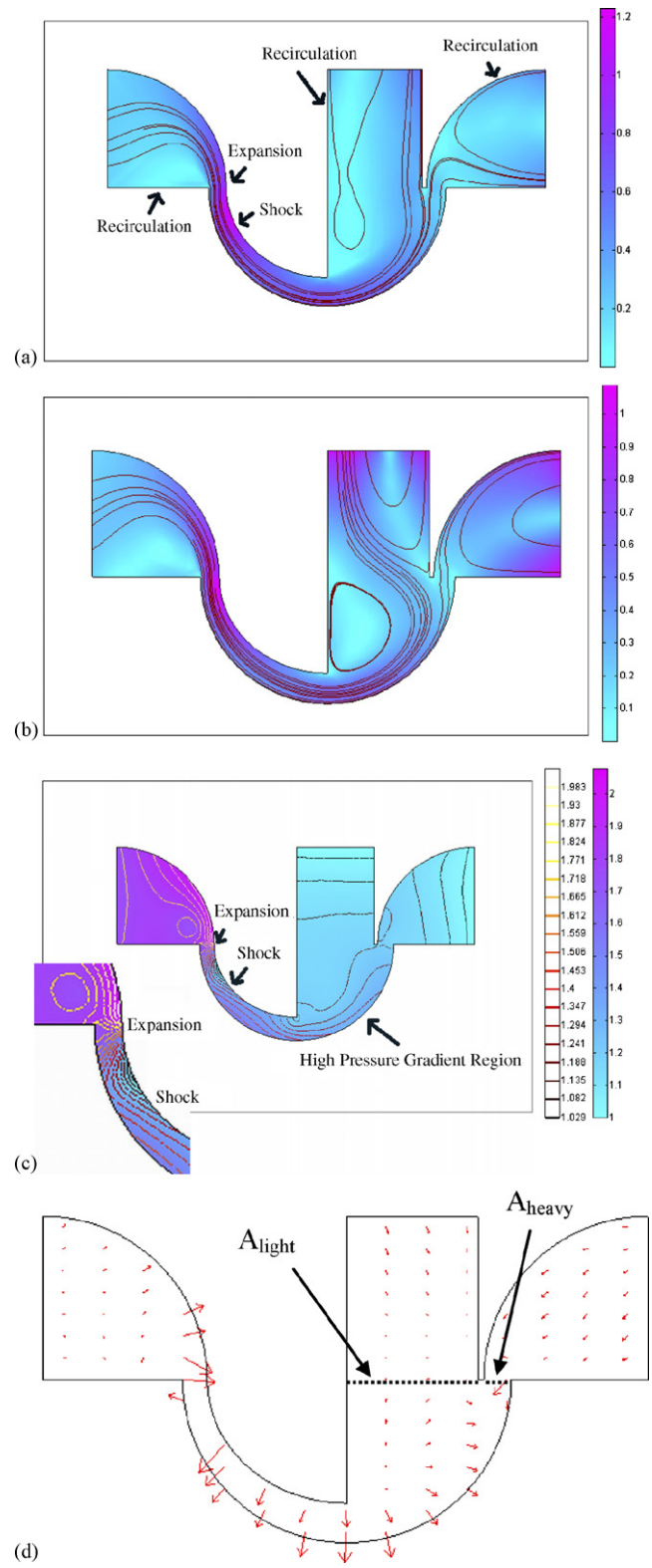

Fig. 7. (a) Mach number distribution, streamlines, and flow structures in device 1 associated with Mode 1; (b) Mach number distribution, streamlines, and flow structures in device 1 associated with Mode 2; (c) total pressure distribution (right scale) and static pressure contours (left scale) in device 1 for flow Mode 1 and a pressure ratio of 1.75; (d) mass diffusive flux vectors for SF_6 in device 1 and Mode 1 when the pressure ratio is 1.75. The horizontal lines denote the surfaces across which the mass flux distributions of SF_6 and N_2 are integrated to determine the total mass fluxes.

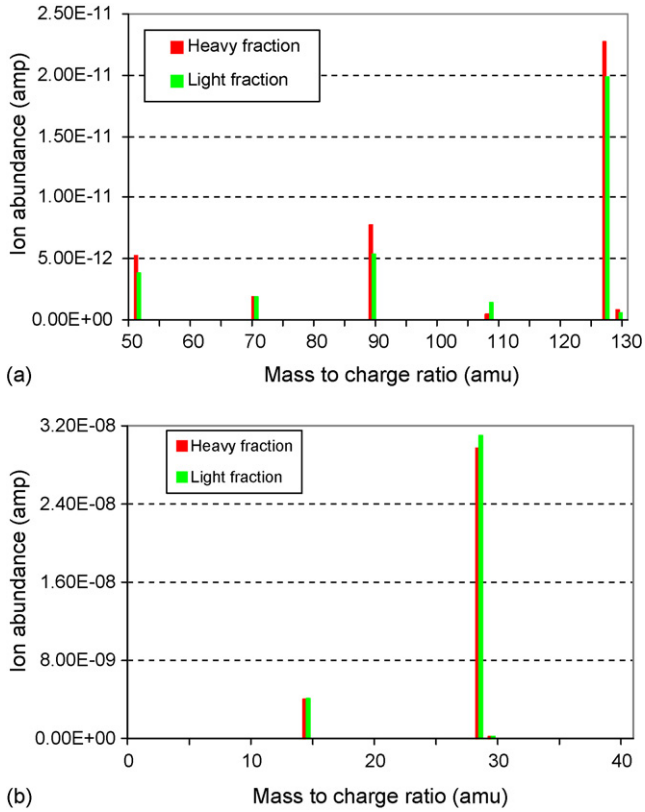

Fig. 8. Comparison of mass spectra of (a) SF_6 and (b) N_2 in the heavy and light fraction streams of device 1.

that separation performance peaks near a device pressure ratio of 2 and decreases monotonically away from the peak. The reason for the peak in separation performance can be inferred from Fig. 10 which shows how the pressure distribution that drives the separation process varies with overall pressure ratio. The figure shows that increasing the pressure ratio increases the magnitude of the pressure gradient in the entrance section of the nozzle that drives SF_6 in an unfavorable direction—i.e. to the inside of the flow passage. At the same time however, increasing the pressure ratio also increases the flow velocity in the remaining 2/3 of the nozzle. This increases the magnitude of the pressure gradient that drives SF_6 in the favorable direction—i.e. to the outside of the flow passage. When the pressure ratio is less than that associated with peak performance, the effect of increased velocity in the nozzle outweighs the effect of the stronger gradients in the nozzle entrance and increasing the pressure ratio improves separation. Conversely, when the pressure ratio is greater than that associated with peak performance, the effects of stronger gradients in the nozzle entrance outweigh the effects of increased velocity in the nozzle and increasing the pressure ratio degrades separation performance.

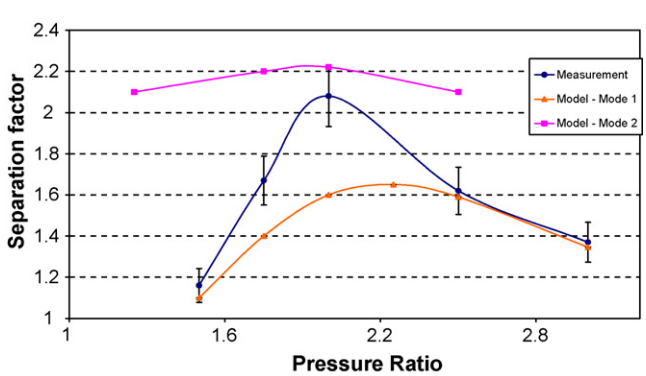

Fig. 9. Comparison of the measured and predicted variations of separation factor with pressure ratio in device 1.

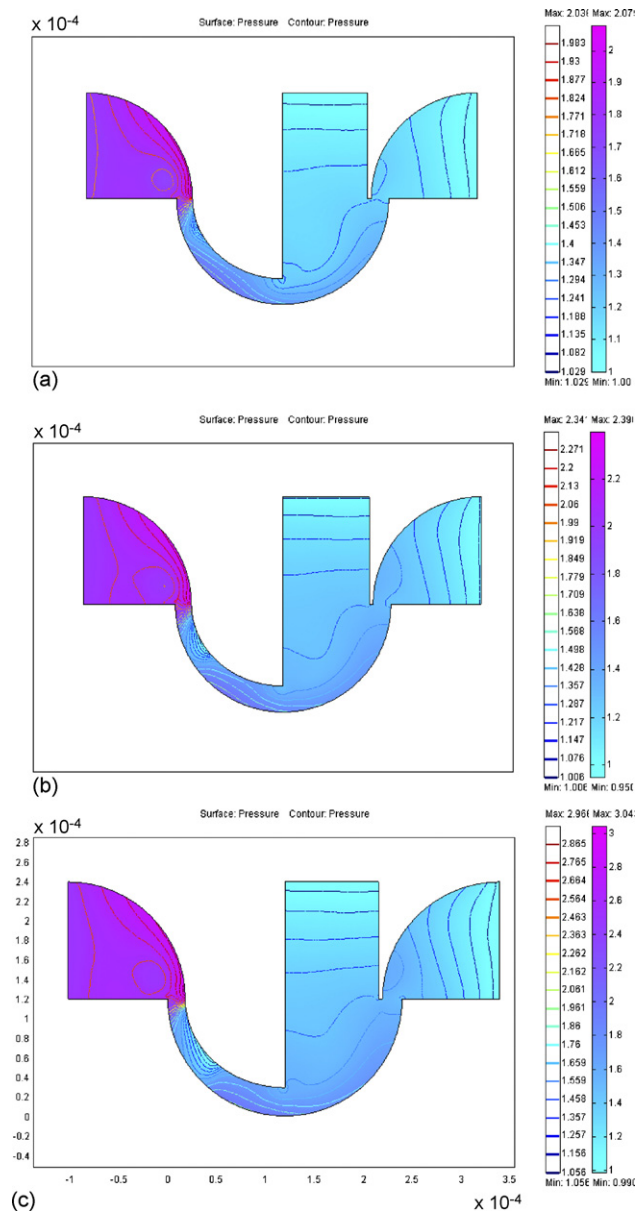

Fig. 10. Simulated pressure distributions in device 1 for Mode 1 at three different pressure ratios (a) 1.75; (b) 2.0; and (c) 2.5.

Fig. 9 also shows that the separation performance predicted by the CFD simulations depends upon the flow mode. While the Mode 1 results match the experimental measurements within the level of experimental uncertainty at pressure ratios below 1.6 and above 2.4, the peak separation performance is more consistent with Mode 2. The reason for Mode 2's superior performance can be inferred from Fig. 7b which shows that Mode 2 has a

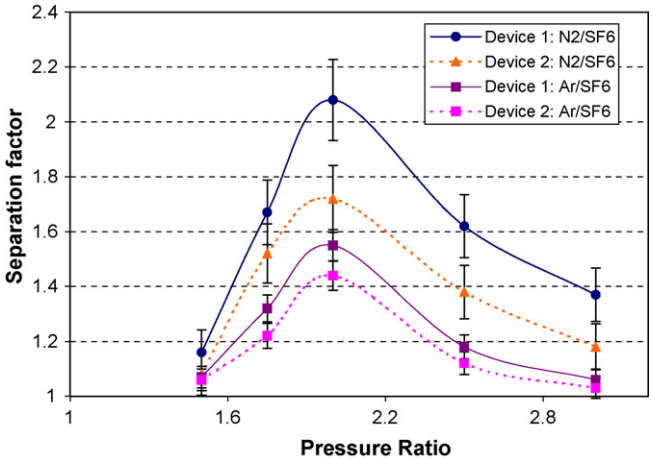

Fig. 11. Measurements of separation factor for two different gas mixtures, N_2/SF_6 and Ar/SF_6, in the two different devices.

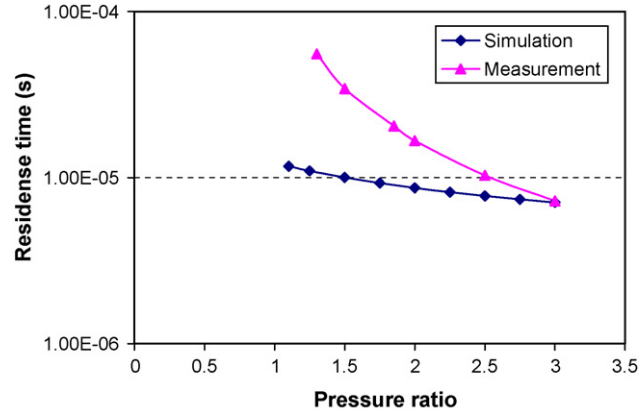

Fig. 12. Simulated residence time versus pressure ratio in comparison with the estimates from the mass flow measurements.

fourth recirculation region that forms downstream of the skimmer in the light fraction stream. This increases the curvature of the streamlines in the deflection region which increases the magnitude of the pressure gradient and drives more SF_6 radially outward.

Why the measurements lie between the predictions of the Mode 1 and Mode 2 CFD solutions when the pressure ratio is between 1.6 and 2.4 is less clear. One possible explanation is that the flow in the experiment is actually unsteady and that small disturbances cause the flow to switch back and forth between the two modes. In this situation, the relative distance between the experimental measurements and the CFD predictions would indicate the fraction of time spent in each mode. For example, when the pressure ratio is below 1.6 or greater than 2.4, the flow would spend most of its time in Mode 1. However, when the pressure ratio is 2, the flow would spend approximately 80% of its time in Mode 2 and 20% of its time in Mode 1. This issue could be resolved conclusively by using infrared micro-particle image velocimetry [30] to visualize the flow field.

5.5. Effect of device geometry and carrier gas

Fig. 11 shows experimental measurements of separation factors in two different devices operating with two different gas mixtures: N_2/SF_6 and Ar/SF_6. The results show that device 1 achieves better performance for both mixtures and that the peak in performance occurs at a pressure ratio of 2 in all cases. Device 1 performs better because a/r_o is larger which allows for a longer flow path and more time for separation to occur. It should be noted, however, that a/r_o cannot be made arbitrarily large as the geometry and dimensions of the converging-diverging nozzle must be maintained in order to accelerate the gas flow efficiently. Separation is weaker for the Ar/SF_6 mixture because the value of $x_{SF_6} - \omega_{SF_6}$ is smaller. This reduces the magnitude of the pressure diffusion term in Eq. (15) that drives the separation process. Finally, the error bars for the Ar/SF_6 curves are smaller because of the very small concentration of Ar in air. This reduces the sensitivity of the measurements to sample contamination by air.

5.6. Residence time

The response of the device is limited by the flow residence time which can be estimated using the numerical simulations and the experimental measurements. In the simulations, the residence time is determined by measuring the time required for particles to traverse streamlines that originate at the mixture entrance and terminate at one of the outlets. The streamlines are selected so that when taken together they account for a minimum of 95% of the total mass flow rate through the device. The average residence time is determined by computing a weighted average of the traverse-times for each streamline based on the mass flow associated with each streamline. In the experiments, the total mass flow rate of device 1 ranges from 0.05 to 0.52 sccm, which corresponds to nozzle exit velocities ranging from 5.9 to 45.4 m/s computed by assuming that the velocity profile is uniform (i.e. by neglecting the growth of boundary layers in the passage). The physical length of the channel divided by the estimated velocity gives the estimated residence time in the experiments. Fig. 12 shows that the residence times estimated from the experiments are significantly longer than those inferred from the numerical simulations which account for the fact that the velocity distribution across the channel is not uniform. Increasing the pressure ratio reduces the thickness of the boundary layer at the walls and leads to a more uniform velocity distribution. As a result, the residence times estimated from the experiment approach those estimated from the CFD as the pressure ratio is increased. The correspondence between these bulk estimates and the more precise estimates made using the CFD simulation increase our confidence in both the experimental and numerical results. They also demonstrate the fast response of the concentrator element.

6. Future work

While the rapid concentration of heavy molecules in a dilute mixture has been demonstrated, the concentration effect observed in this device is much lower than what can be achieved using other methods like sorbent beds or permeable membranes

[10,31]. However, this can be improved in a number of ways. First, the geometry of the inlet should be changed so that the flow enters the nozzle directly without a 90° turn upstream. This would eliminate the formation of pressure gradients that point radially inward and should improve performance significantly. Second, the single-stage elements investigated here could be cascaded to form a multi-stage preconcentrator whose concentration efficiency increases exponentially with the number of the stages. Therefore, further investigations are required to demonstrate the efficacy of the proposed change to the design of the inlet as well as to investigate the cascading concept, the coupling between cascaded elements, and the pressure losses incurred. As the pressure losses increase, it may also become necessary to incorporate more complicated non-equilibrium effects. Finally, it would be very useful to verify that the two simulated flow modes are actually realized within the device. This could be accomplished in the present device using an infrared micro-PIV technique that is capable of measuring velocity fields through silicon walls [30].

7. Conclusions

A concentrating device for gas sensing applications has been constructed and tested. Measurements of its performance are consistent with the predictions of numerical simulations which show that a greater than two-fold enrichment of SF_6 in dilute SF_6/N_2 mixtures can be achieved with response times of better than 0.01 ms. The simulations show that separation occurs as a result of radial pressure gradients created in curved flow passages. The effects of varying the pressure ratio, passage geometry and the composition of the gas mixture were also investigated. The results show that separation performance is maximized when the pressure ratio is optimum, the difference between the mole fraction and volume fraction of SF_6 is maximum, and the length of the flow path through the device is maximum. The results also indicate that the flow in the device may oscillate between two flow modes. The mode with the more highly curved streamlines has better separation performance because pressure gradients are increased in a direction that is favorable for separation. Separation could be improved further by re-designing the inlet section to eliminate the 90° turn before the nozzle entrance. This would prevent the formation of pressure gradients that drive diffusion in an unfavorable direction. The results of this study can be used to develop concentrator cascades where the number of elements can be adjusted to provide a desired level of concentration. Such devices will enable the development of miniature chemical sensing systems with response times that are sufficient to achieve 'real-time' environmental monitoring.

Acknowledgements

The authors would like to acknowledge Nolan Ballew for his aid in using the cleanroom facility at the Institute of Research for Electronics and Applied Physics (IREAP) at UMD. The mass spectrometric gas analysis was conducted with the help of Mr. Wei Lei, Mr. Laurent Henn-Lecordier, Ms. Yuhong Cai, and Prof. Gary Rubloff of the Department of Materials Science and Engineering at UMD.

References

[1] C.-J. Lu, J. Whiting, R.D. Sacks, E.T. Zellers, Portable gas chromatography with tunable retention and sensor array detection for determination of complex vapor mixture, Anal. Chem. 75 (2003) 1400–1409.
[2] C.B. Freidhoff, R.M. Young, S. Sriram, T.T. Braggins, T.W. O'Keefe, J.D. Adam, H.C. Nathanson, R.R.A. Syms, T.J. Tate, M.M. Ahmad, S. Taylor, J. Tunstall, Chemical sensing using nonoptical microelectromechanical systems, J. Vac. Sci. Technol. A 17 (1999) 2300–2307.
[3] S. Taylor, R.F. Tindall, R.R.A. Syms, Silicon based quadrupole mass spectrometry using microelectromechanical systems, J. Vac. Sci. Technol. B 19 (2001) 557–562.
[4] P. Siebert, G. Petzold, Á. Hellenbart, J. Müller, Surface microstructure/miniaturemass spectrometer: processing and applications, Appl. Phys. A 67 (1998) 155–160.
[5] C.-J. Lu, Z. E.T., A dual-adsorbent preconcentrator for a portable indoor-VOC microsensor system, Anal. Chem. 73 (2001) 3449–3457.
[6] J.W. Grate, M.H. Abraham, Solubility interactions and the design of chemically selective sorbent coatings for chemical sensors and arrays, Sens. Actuators B B3 (1991) 85–111.
[7] M.S. Nieuwenhuizen, A.W. Barendsz, Processes involved at the chemical interface of a SAW chemosensor, Sens. Actuators 11 (1987) 45–62.
[8] G.G. Guilbault, Y. Tomita, E.S. Kolesar Jr., A coated piezoelectric crystal to detect organophosphorous compounds and pesticides, Sens. Actuators 2 (1981) 43–57.
[9] A. Mohacsi, Z. Bozoki, R. Niessner, Direct diffusion sampling-based photoacoustic cell for in situ and on-line monitoring of benzene and toluene concentrations in water, Sens. Actuators B B79 (2001) 127–131.
[10] W.-C. Tian, S.W. Pang, C.-J. Lu, E.T. Zellers, Microfabricated preconcentrator-focuser for a microscale gas chromatograph, J. Microelectromech. Syst. 12 (2003) 264–272.
[11] W.-C. Tian, H.K.L. Chan, S.W. Pang, C.-J. Lu, E.T. Zellers, Multiple-stage microfabricated preconcentrator-focuser for micro gas chromatography system, J. Microelectromech. Syst. 14 (2005) 498–507.
[12] E.W. Becker, W. Ehrfeld, D. Münchmeyer, H. Betz, A. Heuberger, S. Pongratz, W. Glashauser, H.J. Michel, R.V. Siemens, Production of separation-nozzle systems for uranium enrichment by a combination of X-ray lithography and galvanoplastics, Naturwissenschaften 69 (1982) 520–523.
[13] E.W. Becker, W. Bier, P. Bley, W. Ehrfeld, K. Schubert, D. Seidel, Development and technical implementation of the separation nozzle process for enrichment of uranium-235, Am. Inst. Chem. Eng., Sym. Ser. 78 (1982).
[14] W. Ehrfeld, Elements of Flow and Diffusion Processes in Separation Nozzles, Springer-Verlag, Berlin/Heidelberg, 1983.
[15] S. Li, C.B. Freidhoff, R.M. Young, R. Ghodssi, Development of MEMS-based micronozzles for gas separation, presented at Materials Research Society (MRS) Spring Meeting, San Francisco, CA, 2004.
[16] P.H. Oosthuizen, W.E. Carscallen, Compressible Fluid Flow, McGraw-Hill, New York, 1997.
[17] M. Gad-el-Hak, The fluid mechanics of microdevices-the Freeman scholar lecture, J. Fluids Eng. 121 (1999) 5–33.
[18] E.W. Becker, Development of the separation nozzle process for enrichment of uranium, German Chem. Eng. 9 (1986) 204–208.
[19] S. Li, C.B. Freidhoff, R.M. Young, R. Ghodssi, Fabrication of micronozzles using low temperature wafer-level bonding with SU-8, J. Micromech. Microeng. 13 (2003) 732–738.
[20] S. Li, J.J. Park, J.C. Day, G.W. Rubloff, C.P. Cadou, R. Ghodssi, Development of a fast-response microfluidic gas concentrating device, Proc. of the Eurosensors XIX, vol. 2, WA10, Barcelona, Spain, 11–14 September, 2005.
[21] C.G. Herbert, R.A.W. Johnstone, Mass Spectrometry Basics, CRC Press, Boca Raton, 2002.
[22] J.D. Anderson, Modern Compressible Flow with Historical Perspective, McGraw Hill, Boston, 1990.

[23] R.F. Probstein, Physiconchemical Hydrodynamics: An Introduction, John Wiley & Sons, New York, 1994, 38.
[24] C.F. Curtiss, R. Byron Bird, Multicomponent Diffusion, Ind. Eng. Chem. Res. 38 (1999) 2515–2522.
[25] R.J. Kee, Michael E. Coltrin, Peter Glarborg, Chemically Reacting Flow – Theory and Practice, Wiley Interscience, Hoboken NJ, 2003, 526.
[26] FEMLAB Reference Manual, Burlington, MA, 2005.
[27] P. Deuflhard, A modified Newton method for the solution of ill-conditioned systems of nonlinear equations with application to multiple shooting, Numer. Math. 22 (1974) 289–315.
[28] FEMLAB 3.1 Documentation, COMSAL AB.
[29] J. C. Day, Numerical simulation of a microfabricated gas preconcentrator for environmental monitoring, MS Thesis, University of Maryland, College Park, 2005.
[30] K. Breuer, J. Bird, G. Han, A. Westin, K. Johan, Z. Cao, Infrared diagnostics for measuring fluid and solid motion inside silicon microdevices, Microscale Thermophys. Eng. 8 (2004) 169–182.
[31] C.-Y. Peng, S. Batterman, Performance evaluation of a sorbent tube sampling method using short path thermal desorption for volatile organic compounds, J. Environ. Monit. 2 (2000) 313–324.

Biographies

Sheng Li received his Bachelors and Masters both in Materials Science and Engineering from the Central South University of Technology in 1993 and Dalian University of Technology in 1996, respectively. He earned his PhD in Electrical Engineering from the University of Maryland in 2006. He is currently a research engineer at Intel Corporation. His research interests include MEMS and microsystems packaging.

Jonathan C. Day obtained his Bachelors in Engineering Physics from Ohio University in 2003 and his Masters in Aerospace Engineering from the University of Maryland in 2005. He is presently a consulting engineer at Booz Allen Hamilton.

Jung Jin Park received his B.S. degree in Materials Science and Engineering from Hongik University (Seoul, Korea) in 1998. In 2006, he received his PhD degree in Materials Science and Engineering from the University of Maryland. He is currently a postdoctoral researcher at the National Institute of Standards and Technology (NIST). His research interests include microfluidics and bioMEMS.

Christopher P. Cadou earned the B.S. and B.A. from Cornell University in 1989, and the PhD in Mechanical Engineering from UCLA in 1996. After post docs at Caltech and at MIT with the microengine project, he joined the University of Maryland's Department of Aerospace Engineering in 2000. His principal research focuses on the physics of fuel–air mixing and combustion in micro-scale power systems. Other research interests include the development of non-intrusive diagnostic techniques for small-scale reacting systems, compact power systems for small UAVS, small engine performance, micro-igniters for hypersonic propulsion systems, smart material actuated servo hydraulic systems, and micro-fluidic separation systems.

Reza Ghodssi is an Associate Professor in the Department of Electrical and Computer Engineering and the Institute for Systems Research (ISR) at the University of Maryland (UMD). He is also the Director of the *MEMS Sensors and Actuators Lab (MSAL)* and a core faculty member in the *Bioengineering Graduate Program* and the *Maryland NanoCenter* at UMD. His research interests are in the design and development of microfabrication technologies and their applications to microsensors, microactuators, and integrative microsystems for biosensing, PowerMEMS and energy harvesting. Dr. Ghodssi received his B.S., M.S., and PhD degrees in electrical engineering from the University of Wisconsin at Madison, in 1990, 1992 and 1996, respectively. He was a Postdoctoral Associate and a Research Scientist in the Microsystems Technology Laboratories and the Gas Turbine Laboratory at the Massachusetts Institute of Technology (MIT) from 1997 until 1999. He has served as a program co-chairman for the *2001 International Semiconductor Device Research Symposium (ISDRS)* and as a chairman of the "MEMS and NEMS Technical Group" at the *American Vacuum Society (AVS)* from 2002 to 2004. Dr. Ghodssi has over 50 scholarly publications and has received the 2001 UMD George Corcoran Award, the 2002 National Science Foundation CAREER Award, and the 2003 UMD Outstanding Systems Engineering Faculty Award. Dr. Ghodssi is a co-founder of the MEMS Alliance in the greater Washington area and a member of the IEEE, AVS, MRS, ASEE and AAAS societies.